

Atomic Layer Deposition of CsI and CsPbI₃

Alexander Weiß,*[§] Georgi Popov,[§] Elisa Atosuo, Anton Vihervaara, Pasi Jalkanen, Marko Vehkamäki, Markku Leskelä, Mikko Ritala, and Marianna Kemell*



Cite This: *Chem. Mater.* 2022, 34, 6087–6097



Read Online

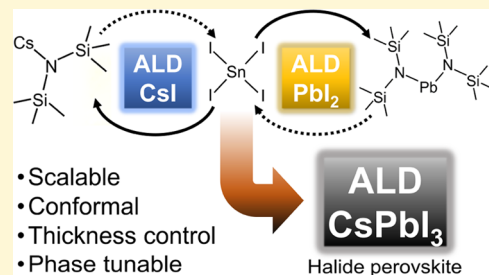
ACCESS |

Metrics & More

Article Recommendations

Supporting Information

ABSTRACT: Cesium iodide (CsI) is a well-established scintillator material that also serves as a precursor for all-inorganic halide perovskite solar absorbers, such as CsPbI₃. However, the lack of conformal and scalable methods to deposit halide perovskite thin films remains a major challenge on their way to commercialization. In this work, we employ atomic layer deposition (ALD) as the key method due to its inherent scalability to large areas and complex-shaped surfaces. We demonstrate two new ALD processes for the deposition of CsI and CsPbI₃ thin films. The CsI process relies on cesium bis(trimethylsilyl) amide (Cs(btsa)) and tin(IV) iodide (SnI₄) as precursors and yields high-purity, uniform, and phase-pure thin films. This process works in a wide temperature range (140–350 °C) and exhibits a large growth per cycle value (GPC) of 3.3 Å (85% of a CsI monolayer). Furthermore, we convert CsI into CsPbI₃ perovskite by exposing a CsI film to our earlier PbI₂ ALD process. We demonstrate the deposition of phase-pure γ - or δ -CsPbI₃ perovskite thin films, depending on the applied deposition temperature and number of PbI₂ cycles. We believe that the ALD-based approach described in this work will offer a viable alternative for depositing perovskite thin films in applications that involve complex high aspect ratio structures or large substrate areas.



INTRODUCTION

Cesium iodide (CsI) is one of the most studied and used scintillator materials. Due to its exceptionally high detective quantum efficiency (DQE), CsI is mainly used in flat-panel-based systems for indirect X-ray imaging in radiology.^{1,2} The outstanding scintillating properties of CsI are based on two reasons: Its band gap, located in the UV region (5.42 eV),³ and its columnar crystal growth, channeling light in the forward direction.⁴ For these reasons, CsI detectors reach DQE values as high as 65%, which is three times higher compared to other detector materials such as powder phosphors.⁵ Moreover, CsI offers further applications, such as in photocathodes⁶ and as part of the electron transport layer in organic solar cells.⁷

CsI thin films are also precursors to some halide perovskites that are used in another important application: perovskite solar cells (PSCs).⁸ CsI thin films can be converted with Pb halides and Sn halides to ternary absorber materials, such as CsPbI₃, CsSnI₃,^{10,11} and Cs₂SnI₆.¹²

In the past decade, researchers have delved into the promising new field of PSCs because of their potential to deliver low-cost solar energy.¹³ Most recently, PSCs reached a power conversion efficiency (PCE) of 25.5%^{14,15} and therefore catch up to the PCE of Si-based solar cells that is around 26%.¹⁶ However, there is a bottleneck of two yet unsolved challenges: First, perovskite thin-film solar cells larger than 10 × 10 cm² remain difficult to manufacture by conventional fabrication methods like spin-coating¹⁷ without sacrificing the film quality. The second unsolved issue lies within the ternary perovskite absorber layer itself, particularly the most studied

and employed methyl ammonium lead iodide CH₃NH₃PbI₃ (MAPI).¹⁸ Although perovskites exhibit exceptional optoelectronic properties that are crucial for solar applications, they suffer from high sensitivity to humidity, temperature, and light in ambient conditions that leads to degradation of the compound.^{19–24} Research has been conducted to address these issues, e.g., by encapsulation, new synthesis routes, and tuning of the perovskite structure by including additives, but no ultimate solution has been found yet.^{25–30}

Our approach to tackle the scalability issue relies on atomic layer deposition (ALD). ALD is a highly controllable method for depositing thin films on large areas and complex-shaped surfaces. It provides uniform and conformal film growth with an accurate control over film thickness and composition.^{31–33} On the downside, ALD is considered to be rather slow and expensive compared to other thin-film techniques. However, its excellent scalability to large areas and batches, or alternatively to roll-to-roll processing,^{34,35} enables high throughput, which offsets its slowness. This is evidenced by the fact that ALD has been in industrial use for decades in large-scale applications, such as electroluminescent displays³⁶ and microelectronics.³⁷ In addition, ALD can be used to form

Received: April 21, 2022

Revised: June 14, 2022

Published: June 27, 2022



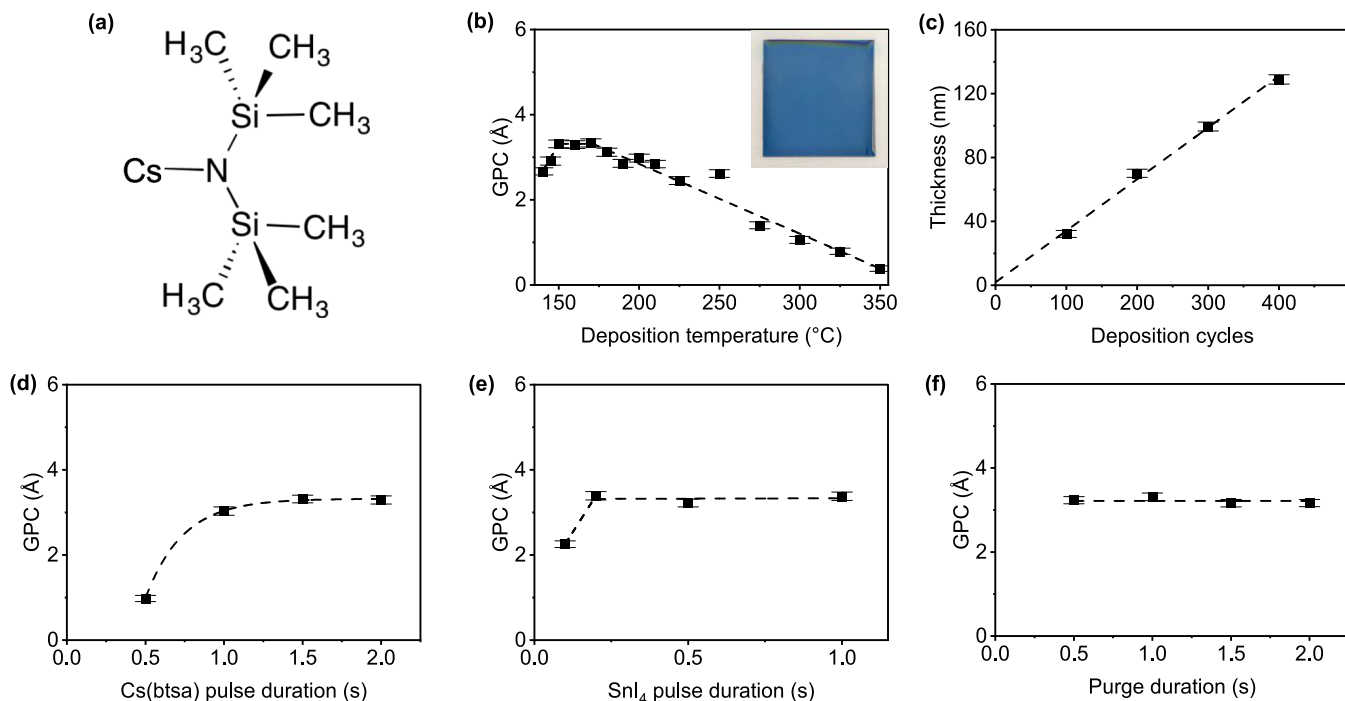


Figure 1. (a) Cesium precursor used in this work (Cs(btsa)). (b) Growth per cycle value (GPC) of CsI films on silicon as a function of deposition temperature, deposited with 300 cycles and pulse durations of 1.5 and 0.5 s for Cs(btsa) and SnI₄, respectively, and 1.0 s purge durations. Inset shows an image of a CsI film on a 5 × 5 cm² Si substrate deposited at 150 °C. (c) CsI film thickness on silicon as a function of applied deposition cycles, deposited at 150 °C, pulse durations of 1.5 and 0.5 s for Cs(btsa) and SnI₄, respectively, and 1.0 s purge durations. (d) GPC of CsI films on silicon as a function of Cs(btsa) pulse duration at 150 °C, SnI₄ pulse and purge durations fixed at 0.5 and 1.0 s, respectively. (e) GPC of CsI films on silicon as a function of SnI₄ pulse duration at 150 °C, Cs(btsa) pulse and purge durations fixed at 1.5 and 1.0 s, respectively. (f) GPC of CsI films on silicon as a function of purge duration at 150 °C, Cs(btsa) and SnI₄ pulse durations fixed at 1.5 and 0.5 s, respectively.

thin films onto high aspect ratio (HAR) substrates.³⁸ This feature enables manufacturing of more complex and efficient devices, which is challenging by conventional methods.

We believe that developing an ALD process for CsI will also contribute to solving the perovskite stability issue. Literature reports give evidence that perovskite solid solutions have better stability than pure perovskites. The key to the improved stability of solid solution perovskites is the controlled addition of several cations (HC(NH₂)₂⁺, CH₃NH₃⁺, Cs⁺) and/or anions (Cl⁻, Br⁻, I⁻) into their structure, which improves the stability of the perovskite against humidity and further increases its photovoltaic activity.^{39–42} Currently, ALD lacks processes to deposit such perovskite solid solutions. Despite the availability of an enormous library of ALD processes,⁴³ only one metal iodide process exists—the PbI₂ process that we developed previously.⁴⁴ PbI₂ films from this process can be converted to MAPI perovskite upon gas treatment. Developing an ALD process for CsI and combining it with the PbI₂ process to deposit CsPbI₃ would be the first step toward depositing solid solution perovskites with ALD from CsPbI₃ with MAPI.

First, to develop an ALD process for CsI, we tried to apply chemistry similar to the one that is used in ALD of some metal fluorides. In these fluoride processes, metal β -diketonates act as the metal precursors and volatile metal fluorides, such as TiF₄⁴⁵ or TaF₅,⁴⁶ act as the fluoride precursors. A ligand exchange between the precursors yields the desired metal fluoride. Analogously, when a volatile metal iodide is used instead of fluoride, the ligand exchange would yield metal iodide. For ALD of CsI, we used commercially available 2,2,6,6-tetramethyl-3,5-heptanedionato cesium (Cs(thd)) as the cesium precursor and titanium(IV) iodide (TiI₄) or

tin(IV) iodide (SnI₄) as iodine precursors. These precursor combinations yielded crystalline CsI at deposition temperatures of 250–350 °C. However, only films that had thicknesses exceeding 400 nm were continuous whereas thinner films had pinholes and gaps in them (Figure S1). Disappointed by this outcome, we hypothesized that lower deposition temperatures would decrease agglomeration and thinner continuous films could be made. However, lower deposition temperatures required a different, more volatile Cs precursor.

In this work, we report a new ALD CsI process that relies on cesium bis(trimethylsilyl) amide⁴⁷ (Cs(btsa)) as the cesium precursor and tin(IV) iodide (SnI₄) as the iodine precursor. The high volatility of Cs(btsa) enables deposition of phase-pure, uniform, and high-purity CsI thin films at low (>140 °C) temperatures. Furthermore, we demonstrate the deposition of ternary CsPbI₃ perovskite thin films with a two-step approach: First, we deposit a CsI thin film via ALD. In the second step, by applying our earlier PbI₂ ALD process on top of CsI, the film is converted into CsPbI₃ perovskite thin film. This combination of CsI and PbI₂ ALD allows us to prepare phase-pure γ -CsPbI₃ and δ -CsPbI₃ thin films.

RESULTS AND DISCUSSION

Film Deposition. We explored CsI film deposition with Cs(btsa) (Figure 1a) and SnI₄ as precursors in the 140–350 °C temperature range (Figure 1b). The lowest deposition temperature was limited by the evaporation temperature of Cs(btsa). Although CsI deposition was still possible at temperatures up to 350 °C, partial Cs(btsa) precursor decomposition was observed at temperatures > 300 °C from

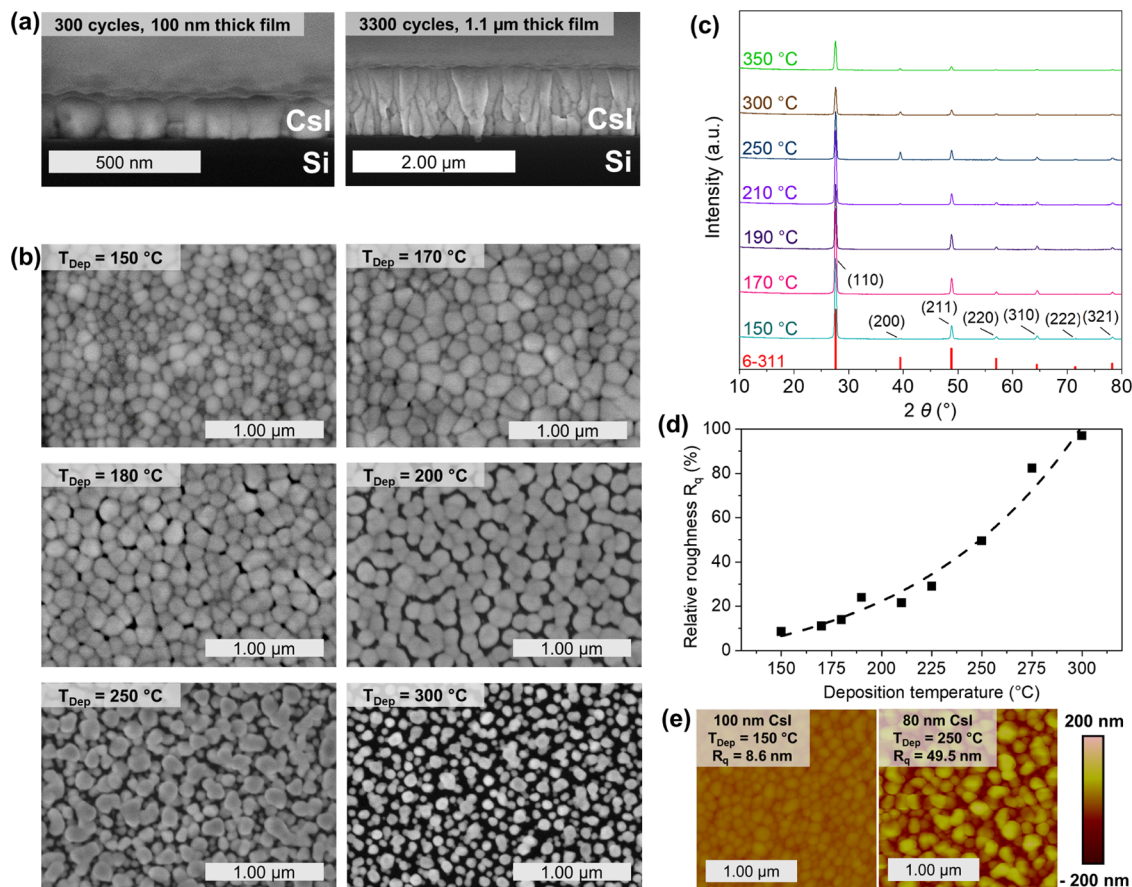


Figure 2. (a) Cross-sectional field-emission scanning electron microscopy (FESEM) images of CsI films deposited on Si with 400 cycles (left) and 3300 cycles (right). (b) Top-down FESEM images of CsI films deposited on Si with 300 cycles at different deposition temperatures T_{Dep} . (c) GIXRD patterns of CsI films on Si deposited at different temperatures. CsI reference pattern ICDD 6-311 is indicated as red bars. (d) Relative atomic force microscopy (AFM) roughness R_q calculated as absolute R_q divided by the film thickness. (e) AFM images of CsI films deposited at 150 and 250 °C. Unless otherwise evident, data are from films deposited with 300 cycles at 150 °C, pulse durations of 1.5 and 0.5 s for Cs(bttsa) and SnI₄, respectively, and 1.0 s purge durations.

a residue built up at the hot end of the precursor delivery tube. In the temperature region between 150 and 170 °C, the growth per cycle value (GPC) was 3.3 Å and was found to be independent of the deposition temperature (so-called ALD window³²). The exceptionally high GPC (85% of one monolayer) results from several factors. First, the monolayer of CsI has a relatively large thickness (3.87 Å) because of the large ionic radii of Cs ($r_{ion,Cs} = 1.81$ Å) and I ($r_{ion,I} = 2.06$ Å).

Second, the chemistry used for CsI deposition, namely, the use of a metal halide as an iodine precursor, enables deposition of up to two monolayers during one ALD cycle. This “double monolayer”-type growth is a typical phenomenon in ALD processes of metal fluorides that use TiF₄ or TaF₅ as fluoride precursors and that also demonstrate exceptionally high GPC.^{45,48–50} For reference, GPC of some metal fluoride ALD processes are tabulated in Table S1.^{45,46,48–53} In the double monolayer-type growth when the precursor is pulsed, it reacts with the second precursor adsorbed on the surface and the desired material is deposited just like in normal monolayer-type growth. The key difference is that during that same pulse, the excess precursor also adsorbs on the surface of the newly formed material. Both precursors behave this way, and the deposition takes place every half-cycle leading to the theoretical maximum of two monolayers per cycle for such processes.

For a detailed study on the influence of the process parameters, we chose the deposition temperature of 150 °C. At this deposition temperature, the GPC saturates with respect to both precursor pulse durations and is independent of the purge durations (Figure 1d–f). As optimal parameters for further depositions, we chose 1.5 and 0.5 s pulse durations for Cs(bttsa) and SnI₄, respectively, as well as 1.0 s purge durations. With these parameters, the thickness depended linearly on the number of applied deposition cycles (Figure 1c). These results are consistent with the behavior typically observed in ALD.

Film Properties. X-ray diffraction (XRD) measurements of CsI films confirm that our process produces crystalline and phase-pure CsI thin films in the whole temperature range (Figure 2c).

Examination by cross-sectional field-emission scanning electron microscopy (FESEM) shows that the films consist of columnar crystallites (Figure 2a). Because scintillator applications usually require film thicknesses up to several micrometers,^{54,55} we demonstrate a deposition of 1.1-μm-thick CsI film in 3.6 h. Thanks to the high GPC of this process—as mentioned above—ALD offers a new and attractive fabrication route for this material. Top-down SEM images show that at deposition temperatures below 180 °C, films are continuous, uniform, and pinhole-free (Figure 2b). As the deposition

Table 1. EDS and ToF-ERDA Composition Analysis of ALD CsI Thin Films^a

sample	cycles	I/Cs ratio (EDS)	element atom % (ToF-ERDA)
Si/CsI (stored in inert atmosphere, transfer through air)	400	1.08	H 1.2 C 0.7 N 0.25 O 2.1 Cs and I 95.7
Si/CsI (stored open in ambient air at \leq 20% RH for 7 days)	300	1.04	H 1.8 C 0.97 N 0.16 O 2.3 Cs and I 94.8
Si/CsI (stored open in ambient air at \leq 40% RH for ca. 42 days)	300	4×10^{-4}	H 19.5 C 25.1 N < 2.0 O 32.7 Cs and I 20.7

^aFilms deposited at 150 °C, pulse durations 1.5 and 0.5 s for Cs(btsa) and SnI₄, respectively, and purge durations 1.0 s. For more details on the composition, see Figure S2.

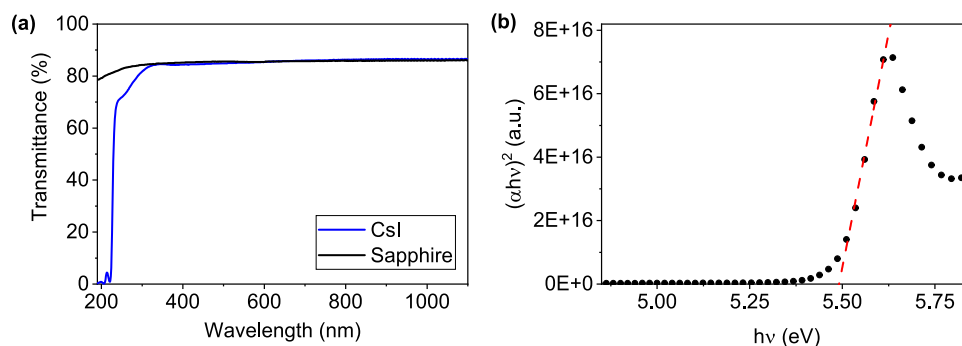
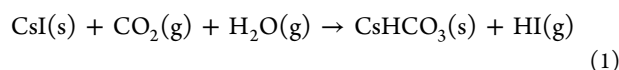


Figure 3. (a) Transmittance spectra of a 100 nm CsI film on sapphire and bare sapphire substrate. (b) Tauc plot of the CsI film in panel (a). The CsI film was deposited at 150 °C, pulse durations were 1.5 and 0.5 s for Cs and I precursors, respectively, and 1.0 s purge durations.

temperature increases to 180 °C and above, the GPC drops and films deposited with the same number of cycles start to become thinner and discontinuous. SEM images reveal the appearance of pinholes in these films. Film roughness measured by atomic force microscopy (AFM) reflects the changes occurring in the film morphology (Figure 2d,e). At 150 °C, the films are relatively smooth ($R_q = 8.6$ nm). As the deposition temperature increases toward 180 °C, the roughness gradually increases due to larger growth of grains. At deposition temperatures ≥ 180 °C, pinholes and film discontinuity cause an even larger increase of the roughness. Characterization of film composition with energy dispersive X-ray spectroscopy (EDS) and time-of-flight elastic recoil detection analysis (TOF-ERDA) showed that the films are stoichiometric CsI (Table 1). Assessing the concentrations of all elements of interest required a combination of the two methods. For Cs, Sn, and I contents, we relied on EDS because the masses of these elements were too close to resolve their individual concentrations from the TOF-ERDA data. No Sn was observed with EDS, and the Cs to I ratios were close to 1:1. TOF-ERDA, in turn, provided light element concentrations. There was a small amount (<5 atom %) of light element impurity in the films. Most notably, oxygen was present even though the precursors are oxygen-free. CsI is known to be hygroscopic.^{56–58} Although we stored the films in either dry or inert conditions, they were still exposed to ambient air during transfer and sample preparation. CsHCO₃

reflections appeared in the XRD pattern of the film stored in ambient air for more than a month (Figure S3). Upon exposure to ambient air, CsI films react with CO₂ and H₂O to produce CsHCO₃ (eq 1). Gradual reaction of CsI into CsHCO₃ in ambient air accounts for the H, C, and O impurities in the films and the decrease in the I content. Heating the reacted film in an inert atmosphere does not restore its original state because of the partial loss of iodine in the reaction (Figure S4).



The optical properties of the ALD CsI films are in good agreement with those reported in the literature. The films are transparent in the visible range (Figure 3a) and absorb in the UV range. We attribute this absorption to the band gap absorption of CsI. The band gap, extracted from the Tauc plot^{3,59,60} (Figure 3b) is 5.49 eV (lit. 5.43 eV⁶¹) and the refractive index is 1.80 ($\lambda = 580$ nm) (lit. 1.78 at $\lambda = 579$ nm).⁶²

Capacitance measurements of ALD CsI thin films resulted in a dielectric constant of 6.8. This is close to the dielectric constant for bulk CsI (6.3) reported in the literature.⁶³

Deposition of CsPbI₃. We prepared CsPbI₃ films by depositing PbI₂ with ALD on top of CsI films. The supercycle approach, a common way to deposit ternary compounds with ALD, was inapplicable in our case. The supercycle approach

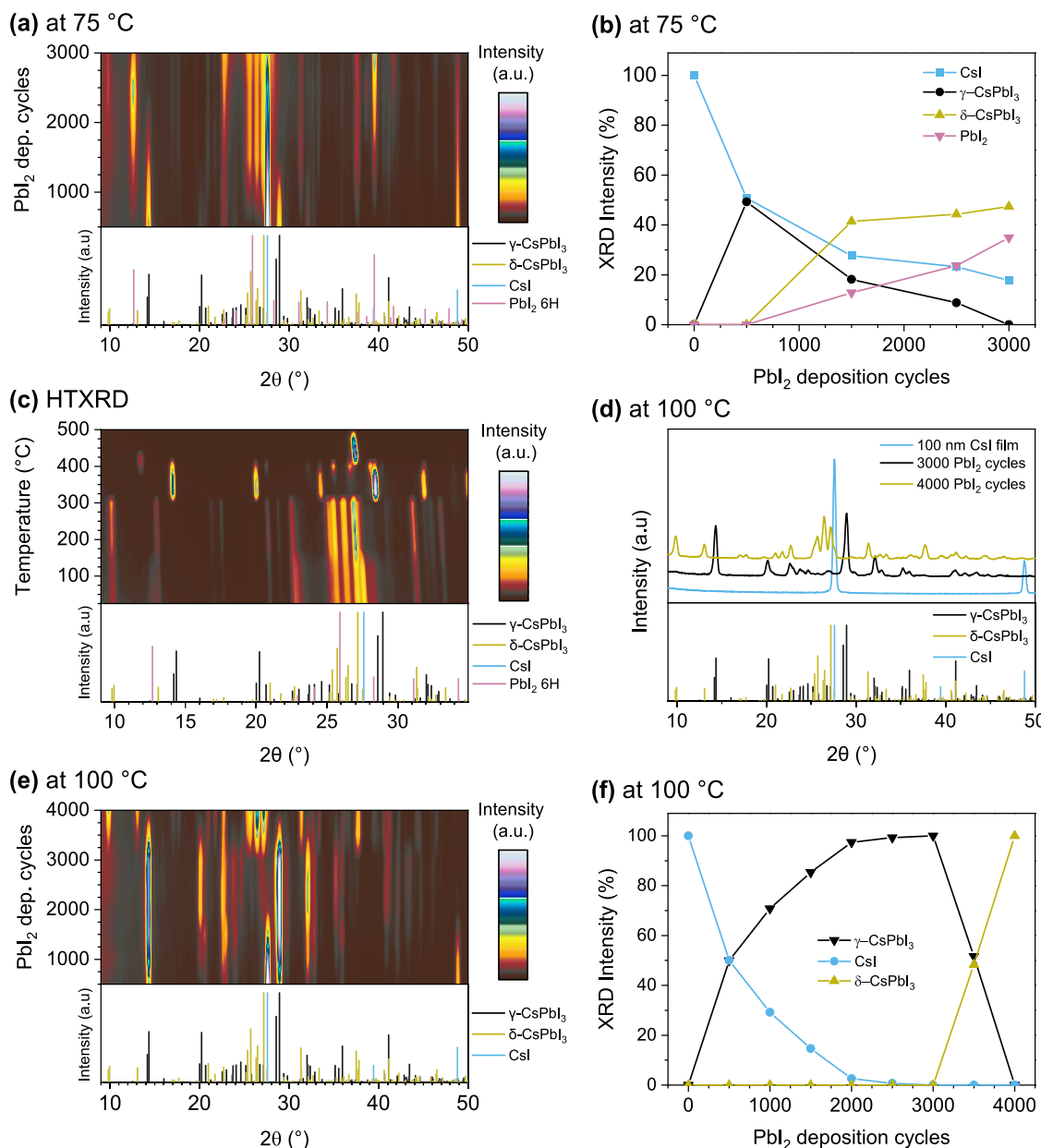


Figure 4. (a) Contour plot of XRD patterns measured from CsI films on which PbI_2 was deposited with different number of cycles at 75 °C. (b) Relative intensity (peak area) of different phases in the patterns from panel (a) as a function of the number of PbI_2 deposition cycles. (c) Contour plot of XRD patterns measured during an anneal of the CsI film after 3000 PbI_2 deposition cycles at 75 °C. (d) XRD patterns of CsI films after 3000 and 4000 PbI_2 deposition cycles at 100 °C. The as-deposited CsI film pattern is also shown for reference. (e) Contour plot of XRD patterns measured from CsI films on which PbI_2 was deposited with different number of cycles at 100 °C. (f) Relative intensity (peak area) of different phases in the patterns from panel (e) as a function of the number of PbI_2 deposition cycles. CsI films (100 nm) were deposited at 150 °C with 300 cycles. The pulse durations were 1.5 s for Cs(bt₄Sn) and 1.0 s for SnI₄ and purge durations were 1.0 s. In the PbI_2 deposition, the durations of the precursor pulses were 0.8 and 2.0 s for Pb(bt₄Sn) and SnI₄, respectively, whereas purge durations were 1.0 s.

relies on alternating deposition cycles of the binary constituents of the desired ternary compound. Therefore, it requires a temperature at which both binary constituent processes work.

In the PbI_2 ALD process, deposition on Si occurs at temperatures below 90 °C and Pb precursor decomposition starts near 150 °C. Because CsI deposition occurs at 140 °C and above, there is no temperature that can be exploited for CsPbI₃ deposition with the supercycle approach. Furthermore, in our previous work,⁶⁴ we observed that in our ALD reactors, PbI_2 films sublime at temperatures above 100 °C. Hence, the only remaining pathway to deposit CsPbI₃ films with these two

processes was the two-step approach where PbI_2 is deposited on top of a CsI film.

Our two-step approach had potential conceptual challenges as well. In essence, it is a solid-solid reaction that would yield stoichiometric CsPbI₃ only when the amounts of CsI and PbI_2 films are equal (eq 2). This would require knowledge of the GPC of PbI_2 on CsI. But if PbI_2 , after being formed, immediately reacts with CsI, then estimating the PbI_2 GPC would be difficult. For this reason, instead of attempting to estimate the GPC of PbI_2 and trying to hit the specific amount of substance that would yield stoichiometric CsPbI₃, we performed a series of depositions with different numbers of

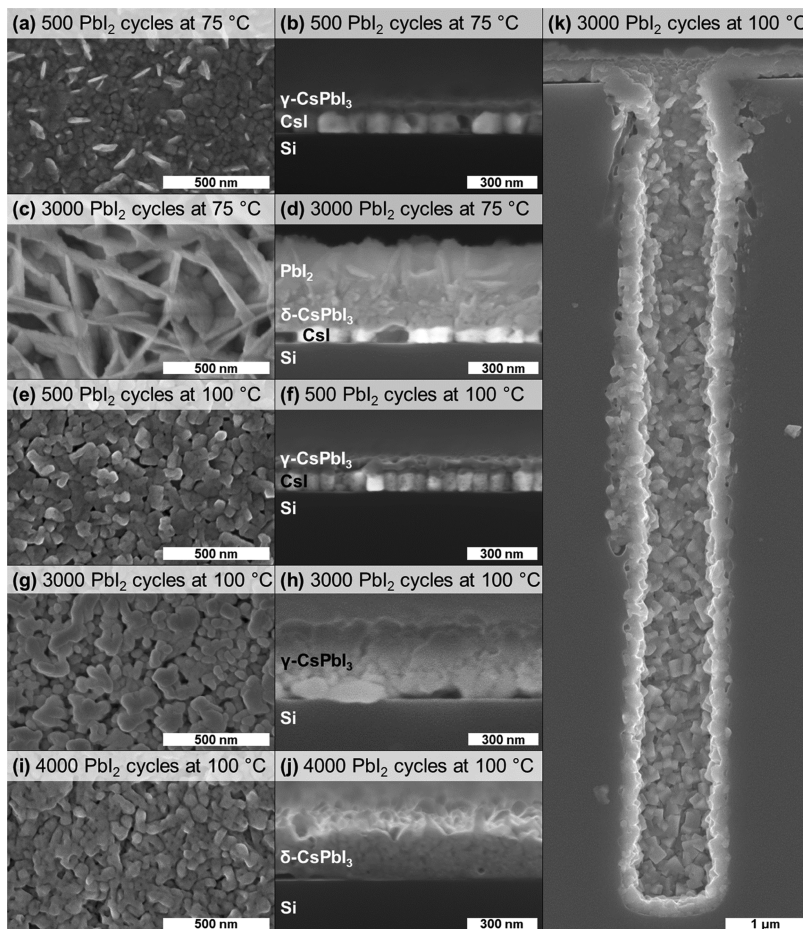


Figure 5. Panels (a), (c), (e), (g), and (i) show top-down SEM images of samples where PbI_2 was deposited on top of the CsI film. Panels (b), (d), (f), (h), and (j) show cross-sectional SEM images of the same samples. Panel (k) shows a cross-sectional FESEM image of a hole with 10:1 AR in a patterned Si substrate. Similar to the other samples, also on this sample, CsI film was deposited first, followed by PbI_2 deposition. CsI films (100 nm) were deposited at 150 °C with 300 cycles. The pulse durations were 1.5 s for $\text{Cs}(\text{btsa})$ and 1.0 s for SnI_4 and purge durations were 1.0 s. In the PbI_2 deposition, the durations of the precursor pulses were 0.8 and 2.0 s for $\text{Pb}(\text{btsa})_2$ and SnI_4 , respectively, whereas purge durations were 1.0 s.

PbI_2 deposition cycles. This experimental series also allows us to observe what happens if the amount of PbI_2 deposited is insufficient or is in excess. We exploited XRD to study the changes in the phase composition.



At 75 °C, the optimal temperature for the ALD PbI_2 process,⁴⁴ the depositions failed to produce phase-pure CsPbI_3 perovskite (Figure 4a,b). Perovskite phase (γ) of CsPbI_3 does form when insufficient amount (500 cycles) of PbI_2 is deposited, but the conversion is not complete and unreacted CsI is still present. Depositing more PbI_2 causes the formation of $\delta\text{-CsPbI}_3$, a nonperovskite phase. The δ -phase replaces the perovskite γ -phase as more PbI_2 is deposited. However, conversion does not proceed to completion: PbI_2 starts to accumulate as a separate phase whereas CsI and $\delta\text{-CsPbI}_3$ remain almost unchanged. Such a film stack, that contains unreacted PbI_2 , CsI , and $\delta\text{-CsPbI}_3$, can still be converted into phase-pure $\gamma\text{-CsPbI}_3$ by annealing under nitrogen at ≥ 325 °C (Figure 4c). However, we were dissatisfied with this outcome as it introduces an extra non-ALD step and significantly increases the highest processing temperature used.

Increasing the PbI_2 deposition temperature to 100 °C enables preparation of phase-pure perovskite $\gamma\text{-CsPbI}_3$ films as

well as phase-pure nonperovskite $\delta\text{-CsPbI}_3$ films (Figure 4d). Although PbI_2 does not grow on typical substrates (silicon, glass etc.) at temperatures above 90 °C and even sublimes at higher temperatures, we hypothesized that the case might be different if metal halides are used as substrates. Indeed, in a spin-off experiment, we were able to deposit PbI_2 at 100 °C on ALD LiF ⁵² and AlF_3 films⁵⁰ (Figure S5). These fluorides do not react with PbI_2 , but CsI on the other hand can convert into CsPbI_3 (eq 2). The conversion reaction can immediately consume PbI_2 deposited on CsI , and thus the stability of PbI_2 becomes irrelevant. Indeed, PbI_2 deposition on CsI at 100 °C causes the formation of CsPbI_3 . Three thousand cycles of PbI_2 yield a $\gamma\text{-CsPbI}_3$ film, whereas 4000 cycles yield a $\delta\text{-CsPbI}_3$ film (Figure 4e,f).

Formation of CsPbI_3 occurs via ALD of PbI_2 followed by a solid-solid reaction with CsI (eq 2) rather than a direct reaction of the PbI_2 precursors with CsI . No CsPbI_3 forms when CsI is exposed to either $\text{Pb}(\text{btsa})_2$ or SnI_4 at 100 °C (Figure S6). EDS composition analysis shows that with the increasing number of PbI_2 deposition cycles, lead and iodine concentrations increase, whereas the cesium concentration decreases (Figure S7a). The changes continue until 3000 PbI_2 cycles. At this cycle number, the element concentrations correspond to CsPbI_3 stoichiometry. The film composition remains constant if the number of PbI_2 deposition cycles is

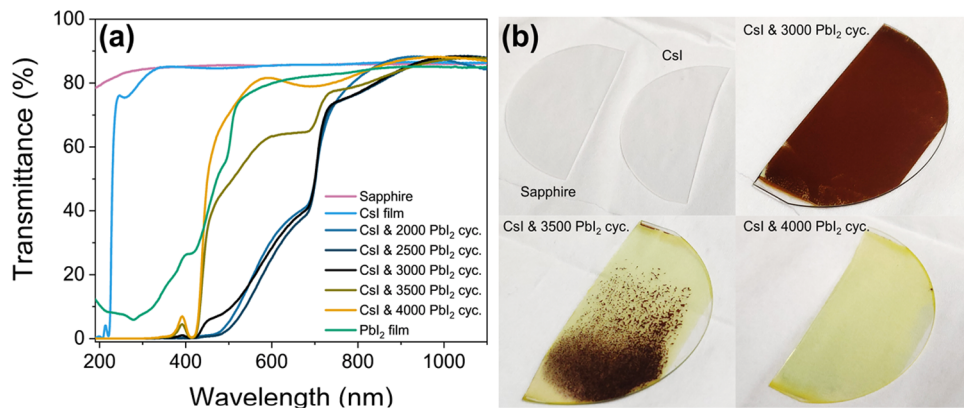


Figure 6. (a) Transmittance spectra of the samples made by depositing CsI on a sapphire wafer and then depositing PbI₂ on CsI. Transmittance spectra of sapphire and the as-deposited CsI film are shown for reference. Measurements were made from the center of the sample. (b) Digital photographs of selected samples from panel (a). CsI films were deposited at 150 °C with 300 cycles. The pulse durations were 1.5 s for Cs(bttsa) and 1.0 s for SnI₄ and purge durations were 1.0 s. In the PbI₂ deposition, the durations of the precursor pulses were 0.8 and 2.0 s for Pb(bttsa)₂ and SnI₄, respectively, whereas purge durations were 1.0 s. The diameter of the sapphire wafers was 5.08 cm.

further increased. The EDS results are in excellent agreement with the XRD data (Figure 4). The composition is independent of the PbI₂ precursor pulse and purge durations, provided they are long enough. Too short pulse or purge times cause incomplete conversion (Figure S7b–d).

We also explored other deposition temperatures for PbI₂ in the 75–130 °C range. These experiments, performed with 3000 PbI₂ cycles, produced only perovskite γ -CsPbI₃ at 100 °C (Figure S8). Films prepared at temperatures higher than 100 °C consisted of both γ - and δ -CsPbI₃ phases, with δ -phase being the dominant one. However, it is possible that γ -CsPbI₃ films can be prepared at those temperatures as well, by optimizing the amount of PbI₂ deposited, as was the case at 100 °C (Figure 4e).

PbI₂ deposition onto CsI films drastically changes their morphology. At 75 °C after 500 cycles of PbI₂, a layer of CsPbI₃ forms on top of the CsI film and scattered flakes of PbI₂ appear on the surface (Figure 5a,b). After 3000 cycles, when viewed top-down, the film resembles a PbI₂ film where PbI₂ flakes form a continuous porous network. However, the cross section reveals a denser CsPbI₃ layer underneath the PbI₂ network and unreacted columnar grains of CsI below CsPbI₃ (Figure 5c,d). In contrast to the experiments at 75 °C, no PbI₂ flakes are present at 100 °C after 500 cycles and only a top layer of CsPbI₃ and unreacted CsI are visible (Figure 5e,f). With more PbI₂ cycles (3000 and 4000), the conversion consumes all of the remaining CsI and the films solely consist of CsPbI₃ (Figure 5g–j). The above observations are in excellent agreement with the XRD data (Figure 4).

We can conclude that at 100 °C, the conversion reaction is self-directing to the stoichiometric CsPbI₃ composition. Only the required amount of PbI₂ needed for the ternary phase formation is deposited, while all of the excess is sublimed away.

As evident from the cross-sectional SEM images (Figure 5), the thickness of the film increases when CsI reacts with PbI₂ (eq 2). The ratio between the thicknesses of fully converted CsPbI₃ and the original CsI can be derived from the amount of substance ratios in the reaction equation and expressions for density, volume, and amount of substance (eq 3, where d is film thickness; for derivation, see Section S1). Equation 3 becomes $d_{\gamma} = 2.49 d_{\text{CsI}}$ and $d_{\delta} = 2.33 d_{\text{CsI}}$ for γ - and δ -CsPbI₃, respectively.

$$d_{\text{CsPbI}_3} = \frac{\rho_{\text{CsI}} M_{\text{CsPbI}_3}}{\rho_{\text{CsPbI}_3} M_{\text{CsI}}} d_{\text{CsI}} \quad (3)$$

The conformality advantage of ALD is retained in our approach for depositing CsPbI₃. Without any process parameter optimizations, we were able to deposit a CsPbI₃ film with a good conformality in holes with 10:1 aspect ratio (AR) (Figure 5k).

Similar to the results on planar substrates, 3000 PbI₂ cycles on a patterned substrate coated with 100 nm CsI film yielded γ -CsPbI₃ (Figure S9). EDS mapping of the patterned substrate cross section shows uniform element distribution through the coating in the structure (Figure S10).

The optical properties of our CsPbI₃ films are in line with the literature. The transmittance of CsPbI₃ films differs radically from the transmittance of CsI films (Figure 6a), which is also reflected in the visual appearance of the films (Figure 6b). Deposition of 3000 cycles of PbI₂ on CsI results in a dark red-brown film with an optical band gap of 1.72 eV (Figure S11a) whereas deposition of 4000 PbI₂ cycles results in a light lime-yellow film with a band gap of 2.85 eV (Figure S11b). These colors and band gap values are typical for the γ - and δ -CsPbI₃ phases, respectively.⁶⁵

CONCLUSIONS

To conclude, we described two new ALD processes for the deposition of CsI and CsPbI₃ thin films. The use of Cs(bttsa) and SnI₄ as precursors yielded phase-pure, uniform, and high-purity CsI thin films in a large deposition temperature range (140–350 °C). The large growth per cycle value (3.3 Å) of this ALD process allows deposition of thicker films in the micrometer range with a reasonable number of deposition cycles. While CsI is a well-established scintillator material for X-ray detector applications, we also demonstrated its conversion into halide perovskite by combining it with our earlier PbI₂ ALD process. At 75 °C, incomplete conversion resulted in a stack of CsI, δ -CsPbI₃ (nonperovskite phase), and PbI₂ films; however, annealing under nitrogen at ≥ 325 °C yielded γ -CsPbI₃ (perovskite phase). At 100 °C, complete conversion took place and formed phase-pure γ - or δ -CsPbI₃ thin films depending on the number of PbI₂ deposition cycles. We believe that the ALD-based approach described in this

work will offer a viable alternative for depositing perovskite thin films in applications that involve complex high aspect ratio structures or large substrate areas.

■ EXPERIMENTAL SECTION

Precursor Synthesis. Cesium bis(trimethylsilyl) amide ($\text{Cs}(\text{btса})$) was synthesized according to Ojeda-Amador et al.⁴⁷ by employing Schlenk line techniques using lithium bis(trimethylsilyl) amide ($\text{Li}(\text{btса})$, 97%, Aldrich) and cesium fluoride (CsF, 99.9%, Aldrich). In short, $\text{Li}(\text{btса})$ dissolved in *n*-hexane was added dropwise to CsF in *n*-hexane over a water bath at 50 °C and left to stir overnight with protection from ambient light. Afterward, the solvent was removed under vacuum and toluene was added. The reaction mixture was filtered and the precipitate was washed with toluene. After removal of the solvent by vacuum, the resulting white product was purified by sublimation to yield white crystals. ^1H NMR (400.144 MHz, 298 K, C_6D_6): δ 0.25 (s, 18 H). ^{13}C NMR (100.616 MHz, 298 K, C_6D_6): δ 7.30.

$\text{Pb}(\text{btса})_2$ was synthesized by employing Schlenk line techniques using PbCl_2 (99.999%, Alfa Aesar) and $\text{Li}(\text{btса})$ (97%, Aldrich), as described in our previous work.^{44,66} $\text{Li}(\text{btса})$ dissolved in tetrahydrofuran (THF) was added dropwise to PbCl_2 in THF over a cold water bath and left to stir overnight with protection from ambient light. THF was removed under vacuum and hexane was added. The reaction mixture was filtered. Hexane was removed from the filtered solution under vacuum over a warm water bath (45 °C), which yielded a red-orange oil. The oil was purified by sublimation under vacuum and the distillate was cooled with liquid nitrogen, which yielded a bright yellow solid that does not melt at room temperature (RT). ^1H NMR (400.144 MHz, 298 K, C_6D_6): δ 0.25 (s, 36 H). ^{13}C NMR (100.616 MHz, 298 K, C_6D_6): δ 5.93.

Film Deposition. Thin films were grown in a commercial cross-flow F-120 ALD reactor (ASM Microchemistry Ltd., Finland) under reduced nitrogen pressure (99.999%, AGA, about 10 mbar) at different temperatures. Nitrogen was used as a carrier and purging gas and led into the reactor through a gas purifier (SAES Pure Gas, MC1-902F, H_2O , O_2 , CO, CO_2 , H_2 , NMHC removal < 1 ppb). Precursor pulsing was realized by inert gas valving. CsI depositions were carried out using solid tin(IV) iodide (SnI_4 , >99%, –10 mesh, ACROS Organics) and the synthesized solid $\text{Cs}(\text{btса})$ as precursors. $\text{Cs}(\text{btса})$ and SnI_4 precursors were sublimed from open quartz boats held inside the reactor at 140 and 75 °C, respectively. For the PbI_2 depositions, the precursor source temperatures were 50 and 62 °C for $\text{Pb}(\text{btса})_2$ and SnI_4 , respectively. Some depositions, described in Figure S1, were made with $\text{Cs}(\text{thd})$ (STREM) and TiI_4 (Alfa Aesar, 99.9%) sublimed at 225 and 105 °C, respectively.

Primarily native oxide-covered 5 × 5 cm² silicon (100) (Si, Okmetic) was used as a substrate for CsI depositions. Additionally, for some depositions, sapphire wafers (2", University Wafer) and tin-doped indium oxide-covered glass (ITO, Glastron) were used as substrates. Sapphire wafers were heated at 1000 °C in an air oven for 2 h to induce atomic step formation.^{67,68} Prior to deposition, all substrates except sapphire were cleaned in an ultrasonic bath, first in a solution of industrial strength cleaning concentrate (Branson) for 20 min at 50 °C, then in H_2O for 10 min at RT, and finally in isopropanol for 10 min at RT. Cleaned substrates were dried in an oven at 100 °C and blown with N_2 .

Film Characterization. Surface morphology of the films was examined with a Hitachi S-4800 field-emission scanning electron microscope (FESEM). Film thicknesses were determined from energy dispersive X-ray spectroscopy (EDS) data measured using an Oxford INCA 350 microanalysis system connected to FESEM. The thicknesses were calculated from the EDS data with GMRFilm software⁶⁹ using the bulk density of CsI (4.51 g/cm³). The errors in thickness values were estimated using weight % uncertainty in the EDS measurements and the propagation of uncertainty expression. Element concentrations were estimated from EDS data using IL_{α} CsL_{α} and PbL_{α} lines.

Light element contents in the films were evaluated with time-of-flight elastic recoil detection analysis (ToF-ERDA) in a 20°/20° geometry using a 45 MeV Au beam or 40 MeV Br beam.

Grazing incidence XRD (GIXRD) patterns were measured with a Rigaku Smartlab diffractometer using a Cu $\text{K}\alpha$ ($\lambda = 1.54 \text{ \AA}$) X-ray beam and parallel beam optics. For CsI films, an incidence angle of 1° was used in the GIXRD measurements. Samples that involved PbI_2 were measured with an incidence angle of 2°. In these measurements, the 2° angle and the orientation of the sample relative to the X-ray beam were chosen based on a series of Ω and φ scans so that the Bragg condition is fulfilled for Si(311) and the corresponding reflection is observed at ca. 54.5° 2θ. This arrangement ensures that the X-ray beam penetrates through the whole thickness of the sample down to the Si substrate.

In situ high-temperature XRD (HTXRD) measurements were conducted with an Anton-Paar HTK 1200N furnace connected to the PANalytical X'pert Pro MPD diffractometer. Before the measurement, the furnace was filled with 99.999% nitrogen and further purified with a MicroTorr MC1-902F gas purifier. Then, the furnace was heated to 300 °C, pumped to 10⁻⁵ mbar, kept there for 1 h, and afterward cooled and filled with nitrogen again. The measurement was done under 50 sccm nitrogen flow. The temperature range was 25–500 °C and the measurements were done with 25 °C intervals. The measurements were conducted using parallel beam optics in the grazing incidence mode (incident angle 2°). The 2θ range was 9–35°.

Optical measurements (UV-vis) were performed with a Hitachi U2000 spectrophotometer. Transmittance spectra measured from samples deposited on sapphire were used for the construction of Tauc plots from which the optical band gaps were estimated.^{59,60} The band gaps of CsI and CsPbI_3 were assumed to be direct allowed.

Atomic force microscopy (AFM) was performed using a Veeco Multimode V instrument. Tapping mode images were captured in air using silicon probes with a nominal tip radius of 10 nm and a nominal spring constant of 3 N/m (RFESP-75 from Bruker). Images were flattened to remove artefacts caused by a sample tilt and a scanner bow. Projected areas were measured from 1 × 1 and 2 × 2 μm^2 images.

The dielectric permittivity of CsI was measured by preparing a simple capacitor structure. A 950 nm CsI layer was deposited on indium tin oxide-coated glass, followed by electron-beam evaporation of Pt top electrodes through a shadow mask. An HP 4284A Precision LCR meter was used to measure the capacitance from which the relative permittivity was calculated using a standard plate capacitor equation.

■ ASSOCIATED CONTENT

SI Supporting Information

The Supporting Information is available free of charge at <https://pubs.acs.org/doi/10.1021/acs.chemmater.2c01202>.

Derivation of an equation for the CsPbI_3 film thickness determination, GPC of published metal fluoride ALD processes, FESEM images of CsI films deposited with $\text{Cs}(\text{thd})$ and SnI_4 , TOF-ERDA element depth profiles of CsI films stored in inert or ambient atmosphere, XRD patterns of the as-deposited CsI film and after being stored in ambient air, contour plot of XRD patterns of a CsI film stored in ambient air, XRD patterns and digital photographs of PbI_2 films deposited at 100 °C on LiF and AlF_3 ALD films, XRD patterns of CsI films before and after exposure to PbI_2 precursors at 100 °C, element concentrations as a function of PbI_2 deposition cycles, precursor pulse and purge durations, contour plot of XRD patterns measured from CsI films on which 3000 cycles of PbI_2 were applied at different deposition temperatures, XRD patterns of a patterned Si substrate after each step during CsPbI_3 coating preparation, EDS element mapping and a linescan of a hole in a patterned

Si substrate coated with CsPbI_3 , and Tauc plots of γ - and $\delta\text{-CsPbI}_3$ thin films on sapphire ([PDF](#))

■ AUTHOR INFORMATION

Corresponding Authors

Alexander Weiß – Department of Chemistry, University of Helsinki, FI-00014 Helsinki, Finland; [orcid.org/0000-0001-5585-2655](#); Phone: +358 406826310; Email: alexander.weiss@helsinki.fi

Marianna Kemell – Department of Chemistry, University of Helsinki, FI-00014 Helsinki, Finland; [orcid.org/0000-0002-3583-2064](#); Phone: +358 504485706; Email: marianna.kemell@helsinki.fi

Authors

Georgi Popov – Department of Chemistry, University of Helsinki, FI-00014 Helsinki, Finland; [orcid.org/0000-0003-1233-8327](#)

Elisa Atosuo – Department of Chemistry, University of Helsinki, FI-00014 Helsinki, Finland

Anton Vihervaara – Department of Chemistry, University of Helsinki, FI-00014 Helsinki, Finland

Pasi Jalkanen – Department of Physics, University of Helsinki, FI-00014 Helsinki, Finland

Marko Vehkamäki – Department of Chemistry, University of Helsinki, FI-00014 Helsinki, Finland

Markku Leskelä – Department of Chemistry, University of Helsinki, FI-00014 Helsinki, Finland; [orcid.org/0000-0001-5830-2800](#)

Mikko Ritala – Department of Chemistry, University of Helsinki, FI-00014 Helsinki, Finland; [orcid.org/0000-0002-6210-2980](#)

Complete contact information is available at:
<https://pubs.acs.org/10.1021/acs.chemmater.2c01202>

Author Contributions

[§]A.W. and G.P. contributed equally to this work.

Notes

The authors declare no competing financial interest.

■ ACKNOWLEDGMENTS

The authors thank the Academy of Finland (Decision Number 330086) and the Finnish Center of Excellence in Atomic layer Deposition (ALDCoE 2012–2017) for financial support. G.P. acknowledges the doctoral program in Materials Research and Nanosciences (MATRENA) of the University of Helsinki as well as Emil Aaltonen and Walter Ahlström foundations for funding and support. The work was conducted in the ALD Center, Finland, infrastructure. The authors thank Dr. Miia Mäntymäki for providing LiF and AlF_3 ALD films.

■ REFERENCES

- (1) Itaya, K.; Shoji, T. Flat Panel Detector. U.S. Patent US2013/0068953 A12013.
- (2) Rong, X. J.; Shaw, C. C.; Liu, X.; Lemacks, M. R.; Thompson, S. K. Comparison of an amorphous silicon/cesium iodide flat-panel digital chest radiography system with screen/film and computed radiography systems—A contrast-detail phantom study. *Med. Phys.* **2001**, *28*, 2328–2335.
- (3) Rai, R.; Singh, B. Optical and structural properties of CsI thin film photocathode. *Nucl. Instrum. Methods Phys. Res., Sect. A* **2015**, *785*, 70–76.
- (4) Zhao, W.; Rowlands, J. A. Amorphous Silicon Detectors. In *Comprehensive Biomedical Physics*; Elsevier, 2014; Vol. 8, pp 315–329.
- (5) Penelope, A.-R.; Williams, J. *Farr's Physics for Medical Imaging*; Saunders Elsevier, 2008.
- (6) Breskin, A. CsI UV photocathodes: history and mystery. *Nucl. Instrum. Methods Phys. Res., Sect. A* **1996**, *371*, 116–136.
- (7) Upama, M. B.; Elumalai, N. K.; Mahmud, M. A.; Wright, M.; Wang, D.; Xu, C.; Haque, F.; Chan, K. H.; Uddin, A. Interfacial engineering of electron transport layer using Caesium Iodide for efficient and stable organic solar cells. *Appl. Surf. Sci.* **2017**, *416*, 834–844.
- (8) Wang, K.; Jin, Z.; Liang, L.; Bian, H.; Bai, D.; Wang, H.; Zhang, J.; Wang, Q.; Liu, S. All-inorganic cesium lead iodide perovskite solar cells with stabilized efficiency beyond 15%. *Nat. Commun.* **2018**, *9*, No. 4544.
- (9) Ahmad, W.; Khan, J.; Niu, G.; Tang, J. Inorganic CsPbI_3 perovskite-based solar cells: A choice for a tandem device. *Solar RRL* **2017**, *1*, No. 1700048.
- (10) Chung, I.; Song, J.-H.; Im, J.; Androulakis, J.; Malliakas, C. D.; Li, H.; Freeman, A. J.; Kenney, J. T.; Kanatzidis, M. G. CsSnI_3 : semiconductor or metal? High electrical conductivity and strong near-infrared photoluminescence from a single material. High hole mobility and phase-transitions. *J. Am. Chem. Soc.* **2012**, *134*, 8579–8587.
- (11) Huang, L.-y.; Lambrecht, W. R. Electronic band structure, phonons, and exciton binding energies of halide perovskites CsSnCl_3 , CsSnBr_3 , and CsSnI_3 . *Phys. Rev. B* **2013**, *88*, No. 165203.
- (12) Qiu, X.; Cao, B.; Yuan, S.; Chen, X.; Qiu, Z.; Jiang, Y.; Ye, Q.; Wang, H.; Zeng, H.; Liu, J.; Kanatzidis, M. G. From unstable CsSnI_3 to air-stable Cs_2SnI_6 : A lead-free perovskite solar cell light absorber with bandgap of 1.48 eV and high absorption coefficient. *Sol. Energy Mater. Sol. Cells* **2017**, *159*, 227–234.
- (13) Rong, Y.; Hu, Y.; Mei, A.; Tan, H.; Saidaminov, M.; Seok, S., II; McGehee, M. D.; Sargent, E. H.; Han, H. Challenges for commercializing perovskite solar cells. *Science* **2018**, *361*, No. 6408.
- (14) Jeong, M.; Choi, I. W.; Go, E. M.; Cho, Y.; Kim, M.; Lee, B.; Jeong, S.; Jo, Y.; Choi, H. W.; Lee, J.; et al. Stable perovskite solar cells with efficiency exceeding 24.8% and 0.3-V voltage loss. *Science* **2020**, *369*, 1615–1620.
- (15) Green, M.; Dunlop, E.; Hohl-Ebinger, J.; Yoshita, M.; Kopidakis, N.; Hao, X. Solar cell efficiency tables (version 57). *Prog. Photovoltaics* **2021**, *29*, 3–15.
- (16) Wu, T.; Qin, Z.; Wang, Y.; Wu, Y.; Chen, W.; Zhang, S.; Cai, M.; Dai, S.; Zhang, J.; Liu, J.; et al. The main progress of perovskite solar cells in 2020–2021. *Nano-Micro Lett.* **2021**, *13*, 1–18.
- (17) Li, Z.; Klein, T. R.; Kim, D. H.; Yang, M.; Berry, J. J.; Van Hest, M. F.; Zhu, K. Scalable fabrication of perovskite solar cells. *Nat. Rev. Mater.* **2018**, *3*, No. 18017.
- (18) Wu, M.; Haji Ladi, N.; Yi, Z.; Li, H.; Shen, Y.; Wang, M. Stability Issue of Perovskite Solar Cells under Real-World Operating Conditions. *Energy Technol.* **2020**, *8*, No. 1900744.
- (19) Manser, J. S.; Saidaminov, M. I.; Christians, J. A.; Bakr, O. M.; Kamat, P. V. Making and breaking of lead halide perovskites. *Acc. Chem. Res.* **2016**, *49*, 330–338.
- (20) Berhe, T. A.; Su, W.-N.; Chen, C.-H.; Pan, C.-J.; Cheng, J.-H.; Chen, H.-M.; Tsai, M.-C.; Chen, L.-Y.; Dubale, A. A.; Hwang, B.-J. Organometal halide perovskite solar cells: degradation and stability. *Energy Environ. Sci.* **2016**, *9*, 323–356.
- (21) Conings, B.; Drijkoningen, J.; Gauquelain, N.; Babayigit, A.; D'Haen, J.; D'Olieslaeger, L.; Ethirajan, A.; Verbeeck, J.; Manca, J.; Mosconi, E.; et al. Intrinsic thermal instability of methylammonium lead trihalide perovskite. *Adv. Energy Mater.* **2015**, *5*, No. 1500477.
- (22) Yang, J.; Siempelkamp, B. D.; Liu, D.; Kelly, T. L. Investigation of $\text{CH}_3\text{NH}_3\text{PbI}_3$ degradation rates and mechanisms in controlled humidity environments using in situ techniques. *ACS Nano* **2015**, *9*, 1955–1963.
- (23) Deretzis, I.; Alberti, A.; Pellegrino, G.; Smecca, E.; Giannazzo, F.; Sakai, N.; Miyasaka, T.; La Magna, A. Atomistic origins of $\text{CH}_3\text{NH}_3\text{PbI}_3$ degradation to PbI_2 in vacuum. *Appl. Phys. Lett.* **2015**, *106*, No. 131904.

- (24) Merdasa, A.; Bag, M.; Tian, Y.; Källman, E.; Dobrovolsky, A.; Scheblykin, I. G. Super-resolution luminescence microspectroscopy reveals the mechanism of photoinduced degradation in CH₃NH₃PbI₃ perovskite nanocrystals. *J. Phys. Chem. C* **2016**, *120*, 10711–10719.
- (25) Gordillo, G.; Torres, O. G.; Abella, M. C.; Peña, J. C.; Virguez, O. Improving the stability of MAPbI₃ films by using a new synthesis route. *J. Mater. Res. Technol.* **2020**, *9*, 13759–13769.
- (26) Siegler, T. D.; Houck, D. W.; Cho, S. H.; Milliron, D. J.; Korgel, B. A. Bismuth Enhances the Stability of CH₃NH₃PbI₃ (MAPI) perovskite under high humidity. *J. Phys. Chem. C* **2019**, *123*, 963–970.
- (27) Ava, T. T.; Al Mamun, A.; Marsillac, S.; Namkoong, G. A review: thermal stability of methylammonium lead halide based perovskite solar cells. *Appl. Sci.* **2019**, *9*, No. 188.
- (28) Fransishyn, K. M.; Kundu, S.; Kelly, T. L. Elucidating the failure mechanisms of perovskite solar cells in humid environments using *in situ* grazing-incidence wide-angle X-ray scattering. *ACS Energy Lett.* **2018**, *3*, 2127–2133.
- (29) Lee, J. W.; Kim, D. H.; Kim, H. S.; Seo, S. W.; Cho, S. M.; Park, N. G. Formamidinium and cesium hybridization for photo-and moisture-stable perovskite solar cell. *Adv. Energy Mater.* **2015**, *5*, No. 1501310.
- (30) Chen, J.; Choy, W. C. Efficient and Stable All-Inorganic Perovskite Solar Cells. *Solar RRL* **2020**, *4*, No. 2000408.
- (31) Miikkulainen, V.; Leskelä, M.; Ritala, M.; Puurunen, R. L. Crystallinity of inorganic films grown by atomic layer deposition: Overview and general trends. *J. Appl. Phys.* **2013**, *113*, No. 021301.
- (32) Ritala, M.; Leskelä, M. Atomic Layer Deposition. In *Handbook of Thin Films*; Elsevier, 2002; pp 103–159.
- (33) Leskelä, M.; Ritala, M. Atomic layer deposition chemistry: recent developments and future challenges. *Angew. Chem., Int. Ed.* **2003**, *42*, 5548–5554.
- (34) Ali, K.; Choi, K.-H. Low-temperature roll-to-roll atmospheric atomic layer deposition of Al₂O₃ thin films. *Langmuir* **2014**, *30*, 14195–14203.
- (35) Hoffmann, L.; Brinkmann, K. O.; Malerczyk, J.; Rogalla, D.; Becker, T.; Theirich, D.; Shutsko, I.; Görn, P.; Riedl, T. Spatial atmospheric pressure atomic layer deposition of tin oxide as an impermeable electron extraction layer for perovskite solar cells with enhanced thermal stability. *ACS Appl. Mater. Interfaces* **2018**, *10*, 6006–6013.
- (36) Kim, Y. S.; Yun, S. J. Studies on polycrystalline ZnS thin films grown by atomic layer deposition for electroluminescent applications. *Appl. Surf. Sci.* **2004**, *229*, 105–111.
- (37) Lee, F.; Marcus, S.; Sherer, E.; Wilk, G.; Swerts, J.; Maes, J. W.; Blomberg, T.; Delabie, A.; Gros-Jean, M.; Deloffre, E. In *Atomic Layer Deposition: An Enabling Technology for Microelectronic Device Manufacturing*, 2007 IEEE/SEMI Advanced Semiconductor Manufacturing Conference; IEEE, 2007; pp 359–365.
- (38) Li, S.; Zhang, P.; Wang, Y.; Sarvari, H.; Liu, D.; Wu, J.; Yang, Y.; Wang, Z.; Chen, Z. D. Interface engineering of high efficiency perovskite solar cells based on ZnO nanorods using atomic layer deposition. *Nano Res.* **2017**, *10*, 1092–1103.
- (39) Ono, L. K.; Juarez-Perez, E. J.; Qi, Y. Progress on perovskite materials and solar cells with mixed cations and halide anions. *ACS Appl. Mater. Interfaces* **2017**, *9*, 30197–30246.
- (40) Xia, X.; Wu, W.; Li, H.; Zheng, B.; Xue, Y.; Xu, J.; Zhang, D.; Gao, C.; Liu, X. Spray reaction prepared FA_{1-x}Cs_xPbI₃ solid solution as a light harvester for perovskite solar cells with improved humidity stability. *RSC Adv.* **2016**, *6*, 14792–14798.
- (41) Tan, H.; Che, F.; Wei, M.; Zhao, Y.; Saidaminov, M. I.; Todorović, P.; Broberg, D.; Walters, G.; Tan, F.; Zhuang, T.; et al. Dipolar cations confer defect tolerance in wide-bandgap metal halide perovskites. *Nat. Commun.* **2018**, *9*, No. 3100.
- (42) Gao, X. X.; Luo, W.; Zhang, Y.; Hu, R.; Zhang, B.; Züttel, A.; Feng, Y.; Nazeeruddin, M. K. Stable and high-efficiency methylammonium-free perovskite solar cells. *Adv. Mater.* **2020**, *32*, No. 1905502.
- (43) Database of Materials Prepared by Atomic Layer Deposition (ALD), 2022. <https://www.atomiclimits.com/alddatabase/>.
- (44) Popov, G.; Mattinen, M.; Hatanpää, T.; Vehkämäki, M.; Kemell, M.; Mizohata, K.; Räisänen, J.; Ritala, M.; Leskelä, M. Atomic layer deposition of PbI₂ thin films. *Chem. Mater.* **2019**, *31*, 1101–1109.
- (45) Pilvi, T.; Hatanpää, T.; Puukilainen, E.; Arstila, K.; Bischoff, M.; Kaiser, U.; Kaiser, N.; Leskelä, M.; Ritala, M. Study of a novel ALD process for depositing MgF₂ thin films. *J. Mater. Chem.* **2007**, *17*, 5077–5083.
- (46) Pilvi, T.; Puukilainen, E.; Kreissig, U.; Leskelä, M.; Ritala, M. Atomic layer deposition of MgF₂ thin films using TaF₅ as a novel fluorine source. *Chem. Mater.* **2008**, *20*, 5023–5028.
- (47) Ojeda-Amador, A. I.; Martínez-Martínez, A. J.; Kennedy, A. R.; O'Hara, C. T. Structural studies of cesium, lithium/cesium, and sodium/cesium bis(trimethylsilyl) amide (HMDS) complexes. *Inorg. Chem.* **2016**, *55*, 5719–5728.
- (48) Pilvi, T.; Puukilainen, E.; Arstila, K.; Leskelä, M.; Ritala, M. Atomic layer deposition of LaF₃ thin films using La (thd) 3 and TiF₄ as precursors. *Chem. Vap. Deposition* **2008**, *14*, 85–91.
- (49) Pilvi, T.; Arstila, K.; Leskelä, M.; Ritala, M. Novel ALD process for depositing CaF₂ thin films. *Chem. Mater.* **2007**, *19*, 3387–3392.
- (50) Mäntymäki, M.; Heikkilä, M. J.; Puukilainen, E.; Mizohata, K.; Marchand, B.; Raisanen, J.; Ritala, M.; Leskelä, M. Atomic layer deposition of AlF₃ thin films using halide precursors. *Chem. Mater.* **2015**, *27*, 604–611.
- (51) Pilvi, T.; Puukilainen, E.; Munnik, F.; Leskelä, M.; Ritala, M. ALD of YF₃ thin films from TiF₄ and Y (thd) 3 precursors. *Chem. Vap. Deposition* **2009**, *15*, 27–32.
- (52) Mäntymäki, M.; Hämäläinen, J.; Puukilainen, E.; Munnik, F.; Ritala, M.; Leskelä, M. Atomic layer deposition of LiF thin films from lithd and TiF₄ precursors. *Chem. Vap. Deposition* **2013**, *19*, 111–116.
- (53) Atosuo, E.; Ojala, J.; Heikkilä, M. J.; Mattinen, M.; Mizohata, K.; Räisänen, J.; Leskelä, M.; Ritala, M. Atomic layer deposition of TbF₃ thin films. *J. Vac. Sci. Technol., A* **2021**, *39*, No. 022404.
- (54) Chen, H.; Gu, M.; Liu, X.; Zhang, J.; Liu, B.; Huang, S.; Ni, C. Simulated performances of pixelated CsI (Tl) scintillation screens with different micro-column shapes and array structures in X-ray imaging. *Sci. Rep.* **2018**, *8*, No. 16819.
- (55) Zhao, W.; Ristic, G.; Rowlands, J. X-ray imaging performance of structured cesium iodide scintillators. *Med. Phys.* **2004**, *31*, 2594–2605.
- (56) Yang, P.; Harmon, C. D.; Doty, F. P.; Ohlhausen, J. A. Effect of humidity on scintillation performance in Na and Tl activated CsI crystals. *IEEE Trans. Nucl. Sci.* **2014**, *61*, 1024–1031.
- (57) Dutta, B.; Singh, B. Influence of humidity on the photoemission properties and surface morphology of cesium iodide photocathode. *Nucl. Instrum. Methods Phys. Res., Sect. A* **2012**, *695*, 279–282.
- (58) Liang, B.; Liu, S.; Guo, L.; Chen, D.; Liu, Y.; Zhong, Z.; Xiong, L. Study of Humidity on the Structure and Optical Properties of Cesium Iodide Thin Film. In *Optics and Photonics for Energy and the Environment*; Optical Society of America, 2015; p ETb3A.6.
- (59) Swanepoel, R. Determination of the thickness and optical constants of amorphous silicon. *J. Phys. E: Sci. Instrum.* **1983**, *16*, No. 1214.
- (60) Sreeman, M.; Sen, S. A simple spectrophotometric method for determination of the optical constants and band gap energy of multiple layer TiO₂ thin films. *Mater. Chem. Phys.* **2004**, *83*, 169–177.
- (61) Rai, R.; Gupta, N.; Jammal, N. F.; Singh, B. Photoemission and optical constant measurements of a Cesium Iodide thin film photocathode. *Nucl. Instrum. Methods Phys. Res., Sect. A* **2015**, *787*, 161–165.
- (62) Rodney, W. S. Optical properties of cesium iodide. *J. Opt. Soc. Am.* **1955**, *45*, 987–992.
- (63) Jones, B. W. The dielectric constant of ionic solids and its change with hydrostatic pressure. *Philos. Mag.* **1967**, *16*, 1085–1096.
- (64) Popov, G.; Bačić, G.; Mattinen, M.; Manner, T.; Lindström, H.; Seppänen, H.; Suihkonen, S.; Vehkämäki, M.; Kemell, M.; Jalkanen,

P.; et al. Atomic Layer Deposition of PbS Thin Films at Low Temperatures. *Chem. Mater.* **2020**, *32*, 8216–8228.

(65) Eperon, G. E.; Paternò, G. M.; Sutton, R. J.; Zampetti, A.; Haghghirad, A. A.; Cacialli, F.; Snaith, H. J. Inorganic caesium lead iodide perovskite solar cells. *J. Mater. Chem. A* **2015**, *3*, 19688–19695.

(66) Gynane, M. J. S.; Harris, D. H.; Lappert, M. F.; Power, P. P.; Rivière, P.; Rivière-Baudet, M. Subvalent group 4B metal alkyls and amides. Part 5. The synthesis and physical properties of thermally stable amides of germanium (II), tin (II), and lead (II). *J. Chem. Soc., Dalton Trans.* **1977**, *20*, 2004–2009.

(67) Yoshimoto, M.; Maeda, T.; Ohnishi, T.; Koinuma, H.; Ishiyama, O.; Shinohara, M.; Kubo, M.; Miura, R.; Miyamoto, A. Atomic-scale formation of ultrasmooth surfaces on sapphire substrates for high-quality thin-film fabrication. *Appl. Phys. Lett.* **1995**, *67*, 2615–2617.

(68) Kim, H.; Ovchinnikov, D.; Deiana, D.; Unuchek, D.; Kis, A. Suppressing nucleation in metal–organic chemical vapor deposition of MoS₂ monolayers by alkali metal halides. *Nano Lett.* **2017**, *17*, 5056–5063.

(69) Waldo, R. An iteration procedure to calculate film compositions and thicknesses in electron-probe microanalysis. *Microbeam Anal.* **1988**, *310*–314.



CAS BIOFINDER DISCOVERY PLATFORM™

PRECISION DATA FOR FASTER DRUG DISCOVERY

CAS BioFinder helps you identify targets, biomarkers, and pathways

Unlock insights

CAS
A division of the
American Chemical Society